Lead-Free High Permittivity Quasi-Linear Dielectrics for Giant Energy Storage Multilayer Ceramic Capacitors with Broad Temperature Stability

WANG, Xinzhen, SONG, Xiaojie, FAN, Yongbo, LI, Linhao, WANG, Dawei, FETEIRA, Antonio <http://orcid.org/0000-0001-8151-7009>, LU, Zhilun, SINCLAIR, Derek C., WANG, Ge and REANEY, Ian M.

ADVANCED ENERGY MATERIALS
www.advenergymat.de

Lead-Free High Permittivity Quasi-Linear Dielectrics for Giant Energy Storage Multilayer Ceramic Capacitors with Broad Temperature Stability

Xinzhen Wang, Xiaojie Song, Yongbo Fan, Linhao Li, Dawei Wang, Antonio Feteira, Zhilun Lu, Derek C. Sinclair, Ge Wang, and Ian M. Reaney**

Electrostatic energy storage capacitors are essential passive components for power electronics and prioritize dielectric ceramics over polymer counterparts due to their potential to operate more reliably at > 100 °C. Most work has focused on non-linear dielectrics compositions in which polarization (P)/electric displacement (D) and maximum field (E_{max}) are optimized to give values of energy density, 6≤U≤21 J cm^{-3}. In each case however, either saturation (dP/dE = 0, AFE) or "partial" saturation (dP/dE → 0, RFE) of P limits the value of U which can be achieved before breakdown. It is proposed that U can be further improved with respect to relaxors (RFEs) and anti-ferroelectrics (AFEs) by designing high permittivity quasi-linear dielectric (QLD) behaviour in which dP/dE remains constant up to ultrahigh E_{max}. QLD multilayer capacitor prototypes with dielectric layers composed of 0.88$NaNb_{0.9}Ta_{0.1}O_3$-0.10$SrTiO_3$-0.02$La(Mg_{1/2}Ti_{1/2})O_3$ deliver room temperature U ≈ 43.5 J cm^{-3}, supporting an extremely-large E_{max} ≈ 280 MV m^{-1}, both of which exceed current state-of-art by a factor of two for devices based on powder, tape-cast technology. Importantly QLD capacitors exhibit scant variation in U (≈15 J cm^{-3}) up to > 200 °C and robust resistance to cyclic degradation, offering a promising new approach for the development of sustainable technology.

1. Introduction

The last three decades have witnessed the development of wide range of energy storage technologies such as rechargeable Li-ion batteries for mobile devices and electric vehicles. Li batteries have a high energy storage density but a comparatively low power density due to their slow discharge rates (ms).[1] In contrast, electrostatic devices based on ceramic dielectrics have a high power density due to their fast discharge rates (ns) but commercial consumer components based on $BaTiO_3$ (BT) have a low discharge energy density (U ≈ 1–2 J cm^{-3}) in comparison with super capacitors and batteries, coupled with a low operating temperature, <125 °C.[2,3] The low energy density and operating temperature are considered limiting factors in their use in power electronics where such devices are required to operate at high temperature (>150 °C) in parallel with core power

X. Wang, Y. Fan, L. Li, D. Wang, D. C. Sinclair, I. M. Reaney
Department of Materials Science and Engineering
University of Sheffield
Sheffield S1 3JD, UK
E-mail: i.m.reaney@sheffield.ac.uk

X. Wang, X. Song
School of Materials Science and Engineering
Shandong University of Science and Technology
Qingdao 266590, China

L. Li
School of Mathematics and Physics
Beijing University of Chemical Technology
Beijing 100013, China

The ORCID identification number(s) for the author(s) of this article can be found under https://doi.org/10.1002/aenm.202400821

DOI: 10.1002/aenm.202400821

D. Wang
School of Instrumentation Science and Engineering
Harbin Institute of Technology
Harbin 150080, China

A. Feteira
Materials and Engineering Research Institute
Sheffield Hallam University
Sheffield S1 1WB, UK

Z. Lu
School of Chemical and Process Engineering
University of Leeds
Leeds LS2 9JT, UK

G. Wang
Department of Materials
University of Manchester
Manchester M13 9PL, UK
E-mail: ge.wang@manchester.ac.uk

components such as batteries within the engine management system. Ceramics are generally favored over polymer-based dielectrics for electrostatic applications in power electronics due to their greater temperature stability.[4] The high raw material costs in comparison with polymers is offset by large-scale industrial manufacturing based on tape casting and screen printing developed for BT multilayer ceramic capacitors (MLCCs) used in consumer electronics.[5] An MLCC is composed of alternating layers of dielectric ceramics and conducting electrodes. When a voltage is applied across the terminals of a MLCC, the electric field leads to charge accumulation within the dielectric layers. The energy storage performance at high field is evaluated based on the volume of the ceramic layers (thickness dependent) rather than the volume of the devices.

Polarization (P) and maximum applied electric field (E_{max}) are the most important parameters used to evaluate electrostatic energy storage performance for a capacitor. Polarization (P) is closely related to the dielectric displacement (D), $D = \varepsilon_0 E + P$, where ε_0 is the vacuum permittivity and E is applied electric field. D-E loops are perhaps more technically accurate but P-E loops are standard terminology that most of the studies used to assess the materials (via ferroelectric P-E measurements). Relaxor-ferroelectric (RFE)[6–8] and anti-ferroelectric (AFE)[9–11] compositions are considered most promising since the slim hysteresis loop and delayed onset of ferroelectric coupling, respectively, maximize the area to the left of the polarization-electric field (P-E) loop and therefore U. On a microscopic level, critical factors that optimize U include crystal structure, grain size, and electrical homogeneity with researchers generally manipulating these parameters to increase E_{max}, particularly for RFE type dielectrics.[2] For example, high $U \approx 15$ J cm^{-3} at $E_{max} \approx 120$ MV m^{-1} was reported for $BiFeO_3$-$SrTiO_3$ (RFE, BF-ST) based MLCCs,[12] invoked by using dopants and alloying additions to decrease leakage conductivity and promote electrical homogeneity with many similar approaches reported in the literature.[7,8,13–17] One further practical constraint on high E_{max} materials is electrostrain or accumulated mechanical energy. This is particularly true for AFE compositions which risk failure after a number of cycles, due to the field-induced transition from AFE to ferroelectric (FE),[6,18] which induces micro-cracking, particularly along the interfaces between ceramic and internal electrodes. In addition, in RFE compositions such as NBT-0.06BT,[19] high field induces a transition from nano to meso/long-range polar order, accompanied by large electrostrain ($S > 0.5\%$) which within an MLCC is undesirable, leading to mechanical failure. In some RFE compositions optimized for energy density, the local crystal chemistry inhibits long-range polar coupling even at high field, reducing electrostrain, e.g. $Na_{0.5}Bi_{0.5}TiO_3$-$Sr_{0.7}Bi_{0.2}TiO_3$ (NBT-SBT) based MLCCs attain high U~20 J cm^{-3} at E_{max}~100 MV m^{-1} with electrostrain of < 0.2%.[6,20] This phenomenon has been empirically observed but is poorly understood. Further advanced materials characterization techniques, such as in situ poling x-ray/neutron scattering and/or in situ poling scanning transmission electron microscopy, are required to understand the underlying mechanism and further facilitate material design. Despite extensive research, E_{max} of RFE (≤170 MV m^{-1})[13] and AFE (≤145 MV m^{-1})[11] based capacitors, remains significantly lower than polymer-based counterparts (>200 MV m^{-1}). The lower E_{max} is however, counterbalanced by higher polarizability/permittivity (ε_r) in ceramic compositions ($\varepsilon_r > 500$) as opposed to polymers ($\varepsilon_r = \approx 5$–30).[21–24] Currently, the widest temperature-stable, high energy density MLCCs reported is 0.87BT-0.13Bi[$Zn_{2/3}(Nb_{0.85}Ta_{0.15})_{1/3}$]$O_3$, with a range of 25 to 190 °C.[13] In comparison, other lead-free MLCC candidates such as BF-ST and NBT-SBT are unable to withstand temperatures >150 °C.[6,20,25]

One further factor for FE, RFE, and AFE type dielectrics evident in the P-E data but rarely discussed is the polarization saturation effect, **Figure 1**. For class II capacitors typically based on $BaTiO_3$, the decrease in dP/dE as field increases causes a reduction in ε_r known as "tuning". X7R FE $BaTiO_3$ based capacitors are quoted to have a room temperature, low field $\varepsilon_r \approx 2000$[26] but as the dielectric layer thickness (d) decreases in MLCCs (state of the art is <0.5 µm), the field increases (E = voltage/thickness) and ε_r reduces by up to 80% to $300 < \varepsilon_r < 400$, limiting energy storage. Similarly, P of AFE dielectrics saturates when dipoles switch to FE, opposing the direction of the external electric field, thus dP/dE = 0 and energy storage ceases to increase with E.[27] This effect is less pronounced for RFE dielectrics. P remains unsaturated at high field but dP/dE → 0 and increasing E is less effective, ultimately risking dielectric breakdown for only small gains in U.[2] FE $BaTiO_3$ based capacitors, AFE, and RFE systems are therefore not ideal for high field applications and we propose that high ε_r (>500) ceramic exhibiting linear dielectric (LD, dP/dE remain constant) or similar quasi-linear dielectric (QLD, dP/dE not constant but with small deviations) behavior are ideal, provided they have sufficiently high breakdown strength.

Materials exhibiting LD/QLD behavior retain an unsaturated polarization with increasing applied field (dP/dE = k) and exhibit negligible electrostrain compared to AFEs and RFEs, which are favorable features for high-energy-density capacitors. Designing such materials is however, challenging. High permittivity requires high average ionic polarisability within the lattice which typically promotes an FE or AFE instability or an RFE response in which dP/dE = 0 or → 0. Reducing polarisability and using low ε_r, commercial Class I linear dielectrics such $CaZrO_3$ based ceramics[28] leads to QLD or LD behavior but P remains low and U is not optimized. $CaTiO_3$ (CT) based QLD ceramics[29–31] have been reported but with $\varepsilon_r <$ 180, low P (< 0.1 C m^{-2}) and U < 3.5 J cm^{-3} in comparison with RFEs or AFEs ($\varepsilon_r > 500$) and thus they have not to date been considered as desirable candidates for high energy density capacitors.[2,3,32]

Here, we illustrate the design criteria and demonstrate (Figure 1), in compositions based on $NaNbO_3$, a high ε_r (>500) ceramic QLD behavior in which we start from an FE state with polar correlations over a micron scale length, induce a RFE state though compositional modification from long to short range order and finally force QLD behavior through substitutions that reduce further polar coupling to a few unit cells. This design concept differs from that proposed recently on $BiFeO_3$ based ceramic thin films which aim to create a RFE phase with high polarization.[8,33] A recent study on $SrTiO_3$ ceramic thin films seeks to induce a similar polar nanocluster feature however, their permittivity is low (≈135), P is approaching saturation, and the materials are synthesized by physical vapor deposition rather than powder-based methods.[34] Here we have selected $NaNbO_3$ (NN) as an initial composition, since it

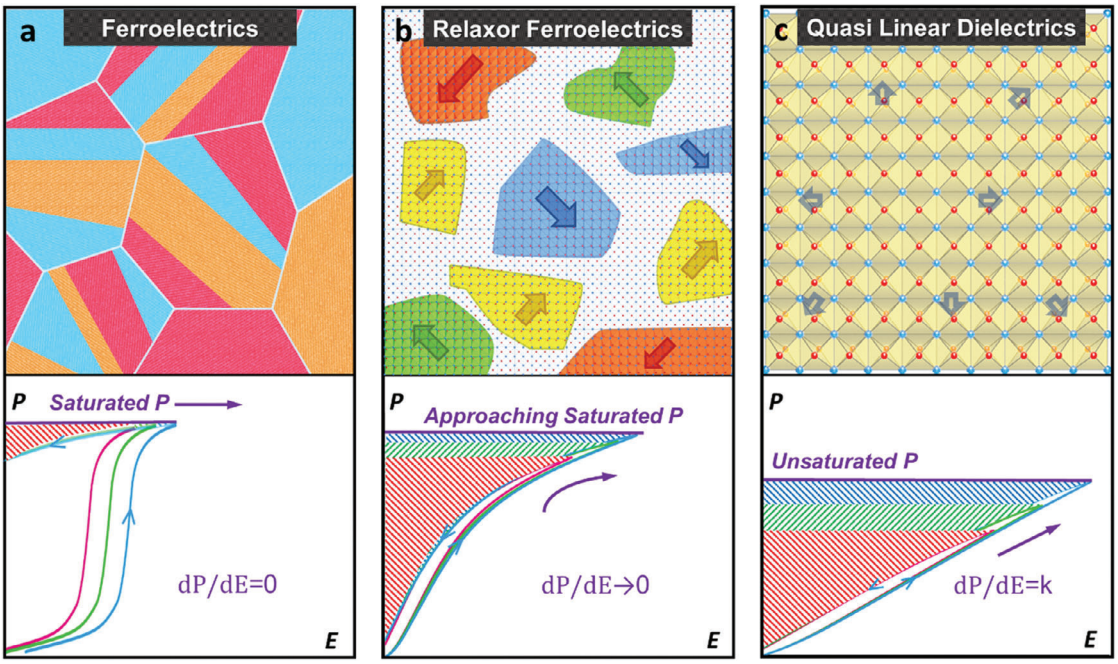

Figure 1. Schematic microstructure and unipolar P-E loops (with a same internal electric between red, green a blue) of different dielectrics for electrostatic energy storage (evaluated by the area of red, green and blue). a) ferroelectric (FE) with macroscopic domains (dP/dE = 0). b) relaxor ferroelectric (RFE) with multiple polar nanoregions (dP/dE → 0). c) Quasi-linear dielectric (QLD) behavior with lattice distortions (dP/dE = constant, k).

has one of the largest known bandgaps amongst perovskites (≈3.4 eV) suggesting a high intrinsic breakdown strength. The B-site contains a highly polarisable d^0 ion and there is a complex sequence of polar and antipolar phases, linked to octahedral tilt transitions, with similar free energies that could lead to frustration within the crystal lattice, thereby inhibiting long-range polar coupling. These factors suggest therefore, that with suitable dopants, NN may be ideal for the synthesis of high ε_r QLDs.

At room temperature (RT), NN has an AFE P phase (*Pbcm* space group, $\sqrt{2}a \times \sqrt{2}a \times 4a$) which coexists with an FE Q phase (*Pmc2*$_1$ space group, $2a \times \sqrt{2}a \times \sqrt{2}a$). The volume fraction of P and Q phases at room temperature along with polarization and dielectric behavior depending process conditions and can also be modified by grain size.[35] On heating, the AFE P undergoes a phase transition to an AFE R phase (*Pnma* space group, $\sqrt{2}a \times 6a \times \sqrt{2}a$) followed by further transitions to the paraelectric S and T phases, before becoming cubic above 600 °C.[36] Forming a binary solid solution of NN with $SrTiO_3$ (ST) stabilizes the FE Q phase [37,38] but substitution of a few mol% $La(Mg_{1/2}Ti_{1/2})O_3$ (LMT) disrupts long-range polar coupling and forces a RFE state with Q phase polar nanoregions (PNRs).[39–41] Substituting Ta (10%) for Nb, decreases the polarizability per unit volume,[42,43] resulting in a material that no longer exhibits RFE behavior near ambient but rather QLD behavior with a frequency-independent plateau in the dielectric response at low temperature.[44] Here, we present the energy storage properties of modified NN-ST compositions and establish, through atomic resolution, high angle annular dark field scanning transmission electron microscopy (HAADF-STEM) and X-ray diffraction, crystallo-chemical principles that lead to high ε_r QLD behavior.

2. Results and Discussion

2.1. Bulk Ceramics

$(0.9\text{-}x)NaNbO_3\text{-}0.1SrTiO_3\text{-}xLMT$ ($0.00 \leq x \leq 0.06$, NN-10ST-100xLMT) and $0.88NaNb_{(1-y)}Ta_yO_3\text{-}0.10SrTiO_3\text{-}0.02LMT$ ($0.05 \leq y \leq 0.15$, $NNTa_y$-10ST-2LMT) were fabricated via solid-state reaction, as detailed in the Experimental Section. A saturated P-E loop is obtained for NN-10ST ceramics with max (P_{max}) and remanent (P_{rem}) of ≈0.33 C m^{-2} and ≈0.22 C m^{-2}, respectively. As the LMT concentration increases, the FE hysteresis loop transforms to a slim P-E loop with a decrease in both P_{max} and P_{rem} compared with NN-10ST, **Figure 2**. The sharp peak in ε_r (≈1400) at 160 °C (433 K) for NN-10ST shifts to lower temperature with reduced magnitude as x increases (Figure S1a–e, Supporting Information). A strong frequency dispersion is observed for NN-10ST-2LMT (Figure S1f, Supporting Information) at −123 °C (150 K) which along with the slim P-E hysteresis loop defines typical RFE behavior. However, X-ray diffraction data (Figure S2, Supporting Information) from NN-10ST-2LMT refines best with *Pnma* ($a^-c^-c^+$ tilt system)[45] rather than $Pm\bar{3}m$ average symmetry that is more typical of RFE ceramics at room temperature (RT),[46] suggesting that although the polar correlation length may be short-range, distortion (tilting) of the O octahedral framework exhibits long-range order, consistent with a low perovskite tolerance factor, $t < 0.97$, where $t = (R_A + R_O)/\sqrt{2}(R_B + R_O)$ in which R_A, R_B and R_O are the average radii of the A, B and O ions, respectively.[47]

As the Ta concentration increased, the B-site polarizability decreased and the broad dielectric maximum at 110 °C (383 K) shifted to below RT whilst still retaining a large ambient ε_r ($\varepsilon_r \approx 544$ for $NNTa_{0.10}$-10ST-2LMT, Figure S3, Supporting

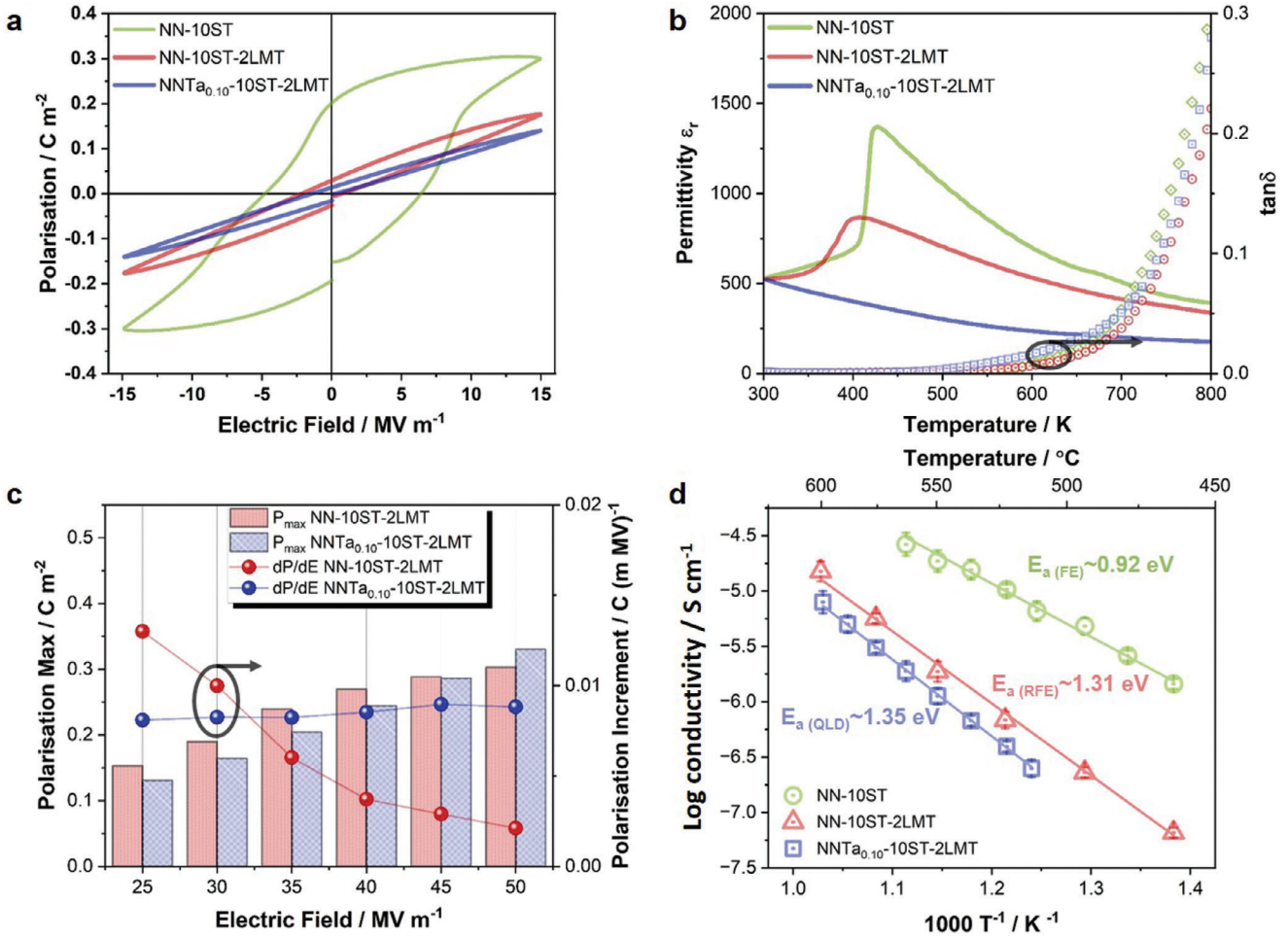

Figure 2. Comparison of ferroelectric, dielectric, and Arrhenius plots of NN-10ST (FE), NN-10ST-2LMT (RFE), and $NNTa_{0.10}$-10ST-2LMT (QLD) bulk ceramics. a) Ferroelectric bipolar P–E loops. b) Permittivity and loss versus temperature. c) Polarization max and increment ratio versus electric field. d) Arrhenius plots of conductivity with associated activation energies.

Information). The low-temperature frequency dispersion observed previously (Figure S1f, Supporting Information) is still present in $NNTa_{0.05}$-10ST-2LMT but is absent for $NNTa_{0.10}$-10ST-2LMT and $NNTa_{0.15}$-10ST-2LMT, as shown in Figure S4 (Supporting Information). The diffuseness of the phase transition for RFE behavior was evaluated using a modified Curie-Weiss law, $1/\varepsilon - 1/\varepsilon_m = (T-T_m)^\gamma/C$, where γ and C are the degree of diffuseness and the Curie constant, respectively. γ was 1.99 for NN-10ST-2LMT which is characteristic of a typical RFE ($\gamma = 2$ for an ideal RFE) but reduced to ≈1.55 for $NNTa_{0.10}$-10ST-2LMT and $NNTa_{0.15}$-10ST-2LMT, suggesting a deviation away from RFE behaviour, as shown in Figure S5a (Supporting Information). The permittivity data were also fitted using a modified Barrett equation, $\varepsilon = C/(\frac{T_1}{2}\coth\frac{T_1}{2T} - T_0)$, to evaluate incipient ferroelectric behaviour, where T_1 is the quantum fluctuation temperature (QFT), T_0 is a FE transition temperature (FTT) and C is the Curie constant.

The ε_r versus T data for $NNTa_y$-10ST-2LMT ($0.05 \le y \le 0.15$) fit the Barrett equation, accounting for the deviation from Curie-Weiss behavior at low temperature, thus indicating possible incipient ferroelectric behavior. T_0 is 103 K for $NNTa_{0.05}$-10ST-2LMT, ≈−55 K for $NNTa_{0.10}$-10ST-2LMT and $NNTa_{0.15}$-10ST-2LMT, Figure S5b–d (Supporting Information) which illustrate that the latter two compositions do not undergo a phase transition to a FE phase at any finite temperature. T_1 for $NNTa_{0.10}$-10ST-2LMT and $NNTa_{0.15}$-10ST-2LMT is ≈217 °C (490 K) which is exceptionally high for a quantum fluctuation effect and requires further investigation. Nevertheless, it is important to consider the possibility of incipient ferroelectric behavior induced by Ta doping that stabilizes a quantum paraelectric (PE) state (at T < QFT) as a mechanism that delivers QLD behavior.[48] The temperature coefficient of capacitance (TCC) for $NNTa_{0.10}$-10ST-2LMT at 100 kHz was evaluated against Z4P, X5R, and X7S criteria from the Electronic Industry Alliance classifications (Figure S6a–c, Supporting Information). tanδ remained <0.01 between −143 to 310 °C (130 to 583 K) and −143 to 290 °C (130 to 563 K) for NN-10ST-2LMT and $NNTa_{0.10}$-10ST-2LMT (Figure S6d, Supporting Information), respectively.

dP/dE, for NN-10ST-2LMT (0.014 C m^{-1} MV^{-1}) and $NNTa_{0.10}$-10ST-2LMT (0.008 C m^{-1} MV^{-1}) were calculated at 25 MV m^{-1} (low-field) to compare the initial polarization saturation behavior between RFE and QLD, Figure 2c. The dP/dE drops by

≈80% to 0.003 C m^{-1} MV^{-1} at 50 MV m^{-1} for NN-10ST-2LMT (RFE) but remains almost a constant for $NNTa_{0.10}$-10ST-2LMT up to E > 50 MV m^{-1} (high-field), confirming QLD behavior. dP/dE = k up to breakdown, has never been achieved in any dielectric bulk ceramics with permittivity (>500) that delivers U (>6 J cm^{-3}). For example, dP/dE drops by ≈81% (from 0.021 to 0.004 C m^{-1} MV^{-1}, Figure S7a, Supporting Information) and ≈45% (from 0.011 to 0.006 C m^{-1} MV^{-1}, Figure S7b, Supporting Information) for 0.62NBT-0.3SBT-0.08Bi($Mg_{2/3}Nb_{1/3}$)O_3 (U = 7.5 J cm^{-3})[20] and 0.50$K_{0.5}Bi_{0.5}TiO_3$-0.42BF-0.08Sm($Mg_{2/3}Nb_{1/3}$)O_3 (U = 6.1 J cm^{-3}),[49] respectively. E_{max} for $NNTa_{0.10}$-10ST-2LMT (QLD) is ≈58 MV m^{-1} compared to ≈46 MV m^{-1} for NN-10ST-2LMT (RFE), giving rise to excellent U = 8.7 J cm^{-3} with η = 80%, one of the highest energy storage performance among all lead-free bulk ceramics (Figure S8, Supporting Information).[12,15,42,50–53] Meanwhile, the current (I) increases slightly and becomes broadening (not peaks yet) near zero field in the I-E loop, Figure S8f (Supporting Information), suggesting non-ferroelectric (either paraelectric or incipient ferroelectric) behavior for $NNTa_{0.10}$-10ST-2LMT.[54]

E_{max} is among one of the highest in the literature due to an electrically homogeneous microstructure with a single highly resistive component with activation energy (≈1.35 eV). All samples, irrespective of the polar correlation length (FE-RFE-QLD), exhibited a single arc in complex impedance, Z* plots (Figure S9a, Supporting Information), and single (overlapping) Debye-like peaks in combined plots of the imaginary components of Impedance, Z'' and electrical modulus, M'' (Figure S9b–d, Supporting Information). Such responses could be modeled (to a first approximation) on a single, parallel Resistor-Capacitor (RC) equivalent circuit which is consistent with a homogeneous electrical microstructure. Furthermore, the M'' Debye-peaks increased with increasing temperature (Figure S10a–c, Supporting Information) which is consistent with a paraelectric/incipient ferroelectric response, thereby confirming the impedance data are dominated by a bulk (grain) response. The temperature-dependent capacitance values, extracted from the M'' peaks, Figure S10d–f (Supporting Information), correlate well with the fixed frequency ε_r data (Figures S1 and S3, Supporting Information), confirming the conductivity to be linked to a bulk (grain) response. A combination of an electrically homogeneous bulk-dominated response and the absence of any significant core-shell or grain boundary contributions inhibits the formation of conducting pathways at high field (E_{max}). This is particularly important when the dielectric layer thickness is reduced during the fabrication of MLCCs. The resistivity at 873 K (600 °C) increased from R_{FE} ≈ 65 kΩ cm (NN-10ST) to R_{RFE} ≈ 560 kΩ cm (NN-10ST-2LMT) and further to R_{QLD} ≈ 790 kΩ cm ($NNTa_{0.10}$-10ST-2LMT), leading to a > x10 reduction in conductivity (Figure 2d; Figure S9a, Supporting Information). The decrease in the bulk-dominated conductivity was accompanied by an increase in activation energy, E_a (calculated from Arrhenius plot, Figure 2d), from $E_{a(FE)}$ ≈ 0.92 eV (NN-10ST) to $E_{a(RFE)}$ ≈ 1.31 eV (NN-10ST-2LMT) to $E_{a(QLD)}$ ≈ 1.35 eV ($NNTa_{0.10}$-10ST-2LMT), further favoring a high E_{max}. Although not fully understood at this stage, LMT has a significant influence on both the carrier concentration and E_a of the bulk conductivity in the ceramics. Such resistivity and activated energy are much higher than BF-ST based but equivalent to NBT-SBT based RFE type dielectrics reported in the literature.[20,52]

The unipolar strain-electric field (S-E) loops of NN-10ST-2LMT (RFE) and $NNTa_{0.10}$-10ST-2LMT (QLD) were evaluated simultaneously with the P-E loops. The electrostrain at E_{max} (>40 MV m^{-1}) for NN-10ST-2LMT (RFE) is over 0.60%, compared with only ≈0.12% for $NNTa_{0.10}$-10ST-2LMT (QLD) (Figure S11a, Supporting Information) suggesting that QLDs have reduced mechanical strain and accumulated mechanical energy with respect to their RFE counterparts, as proposed from our initial design criteria (Figure 1). Electrostrictive S-E loops, Figure S11a,b (Supporting Information), were obtained for $NNTa_{0.10}$-10ST-2LMT (QLD), giving good linear fit versus P^2 with an electrostrictive coefficient (Q) of ≈ 0.006 m^4 C^{-2} (Figure S11c, Supporting Information).

2.2. Advanced Transmission Electron Microscopy of NN-10ST-2LMT (RFE) and $NNTa_{0.10}$-10ST-2LMT (QLD)

Diffraction contrast images and electron diffraction patterns from NN-10ST-2LMT (RFE) and $NNTa_{0.10}$-10ST-2LMT (QLD) are shown in **Figure 3a–c**, respectively. The Dark-Field (DF) image in Figure 3a is obtained using a ½{hk0} superstructure reflection and highlights two types of planar defect in NN-10ST-2LMT (RFE): orientational walls which separate ferroelastic (FElast) domains and antiphase boundaries (APBs) which divide regions of in-phase tilt that have nucleated and impinged out of phase. The orientational domains are not considered to be ferroelectric since NN-10ST-2LMT does not undergo a phase transition that involves the onset of macroscopic spontaneous polarization and they are too large to be attributed to PNRs. Instead, they arise due the need to accommodate the spontaneous strain that accompanies an octahedral tilt transition. Figure 3b shows similar domain structures in $NNTa_{0.10}$-10ST-2LMT (QLD) ceramics with the presence of both APBs and ferroelastic domains.[55] In $NNTa_{0.10}$-10ST-2LMT QLD ceramics, the onset of long-range polar order is suppressed completely and therefore the domain structures are not associated with the onset of a ferroelectric phase transition and relate only the onset of octahedral tilting. Further electron diffraction patterns from NN-10ST-2LMT (RFE) along <011> and <111> showed additional superstructure reflections at ½{hkl} ½{hk0} and ½{00l} positions, with identical patterns obtained from $NNTa_{0.10}$-10ST-2LMT, suggesting that the oxygen octahedral sublattice is distorted through rotations not only in-phase (½{0kl}) but also antiphase {½{hkl} accompanied by reflections arising from antiparallel cation displacements (½{00l}).[55–57] This combination of superstructure reflections is consistent with an $a^-a^-c^+$ tilt system which is ascribed *Pnma* symmetry[58] and agrees with the average macroscopic symmetry obtained by refinement of the X-ray diffraction data (Figure S2b, Supporting Information). The absence of long-range polar order in NN-10ST-2LMT (RFE, Figure 3a) and $NNTa_{0.10}$-10ST-2LMT (QLD, Figure 3b,c) indicates that the oxygen-octahedral distortions do not couple to polarization, presumably due to frustration resulting from competing FE and AFE displacements and perturbation of the local structure through mixtures of ion radii and valence states on the A and B-sites of the lattice. The average tolerance factor of NN-10ST-2LMT (RFE) and $NNTa_{0.10}$-10ST-2LMT (QLD) is <0.97, commensurate with the onset of long-range octahedral rotations significantly above RT. The substitution of Ta

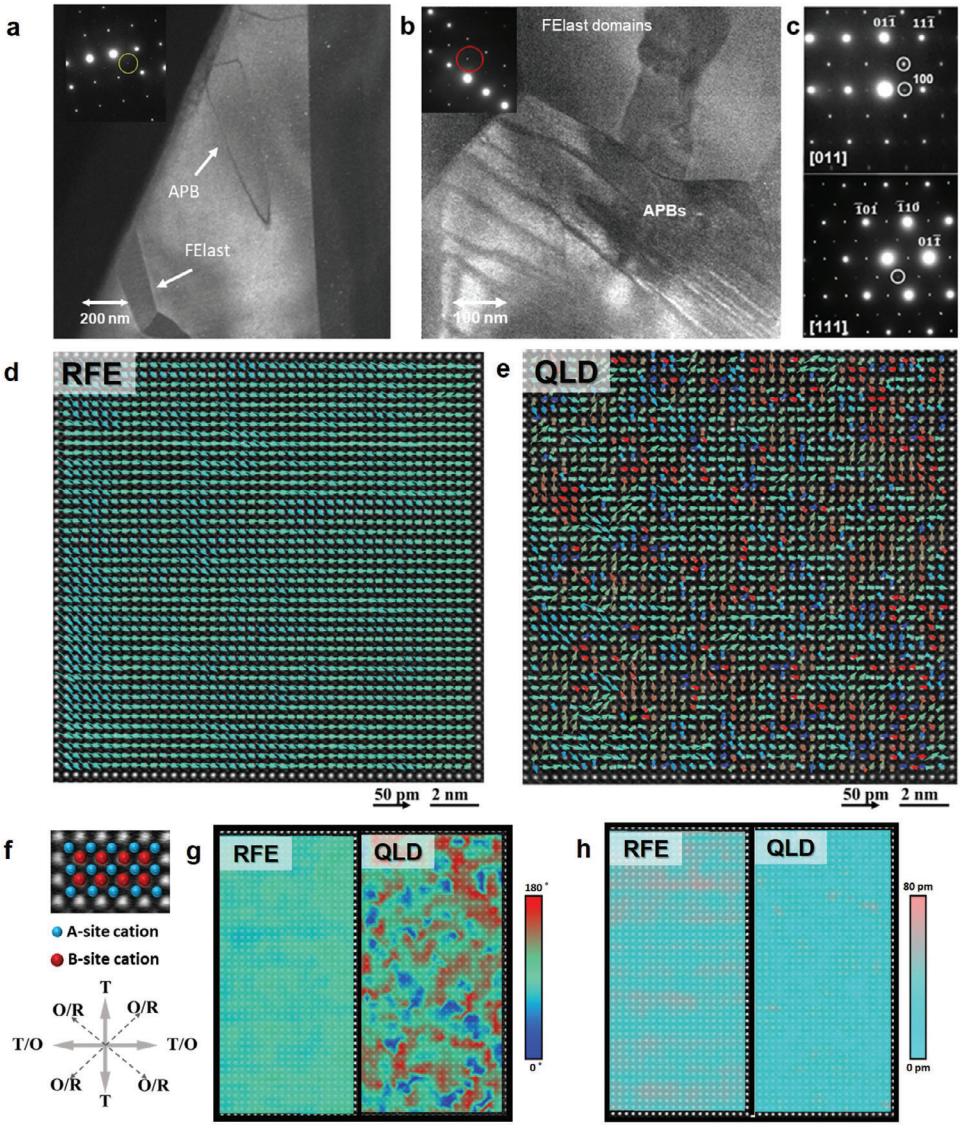

Figure 3. Advanced Transmission Electron Microscopy of RFE type NN-10ST-2LMT and QLD type $NNTa_{0.10}$-10ST-2LMT samples. a) DF image using a ½{hk0} in phase tilt reflection and [001] zone axes from NN-10ST-2LMT superstructure reflections b) DF image using a ½{hkl} antiphase tilt superstructure reflection, inclined to a <110> zone axis showing antiphase boundaries in $NNTa_{0.10}$-10ST-2LMT. Ferroelastic domains are visible in the adjacent grain. c) [011] and [111] zone axes from NN-10ST-2LMT (equivalent patterns were obtained from $NN_{0.10}Ta$-10ST-2LMT). The ringed reflections in the [011] and [111] zone axes are at ½{hkl}, ½{hk0}, and ½{00l} positions and are consistent with antiphase tilting, in phase tilting and antiparallel cation displacements, respectively.[55] The [001]-oriented atomic resolution HADDF-STEM images for d) NN-10ST-2LMT (RFE) and e) $NNTa_{0.10}$-10ST-2LMT (QLD). Individual arrows show B-site cation displacement vectors in individual unit cell with different vector angle. f) The blue and red spheres represent A- and B-site cations, respectively, and schematics of polarization directions for T, R and O structures are also shown. g) The projected polarization angle, and h) polarization magnitude mapping, derived from Figure 3d (REF) and Figure 3e (QLD) and is indicated by contrast differences.

for Nb, has no effect on the tolerance factor ($r_{Nb} = r_{Ta} = 0.64$ Å)[47] but does decrease the average polarisability ($\alpha_{Nb} > \alpha_{Ta}$),[59] consistent with a transformation from a RFE to a QLD state in which displacements from unit cell to unit cell are only weakly coupled if at all (Figure 1).

To further investigate the local polar order in these two samples, atomic resolution HAADF-STEM was carried out, Figure S12 (Supporting Information), followed by analysis of the local displacements.[60] The local distortions from each perovskite ABO_3 lattice were determined by the displacement of the B-site (stronger contrast) relative to the center of the nearest four A-sites (weaker contrast). A- and B-site cations of the perovskite lattice in a [001] projection is shown in Figure 3d (NN-10ST-2LMT, RFE) and Figure 3e ($NNTa_{0.10}$-10ST-2LMT, QLD). The atomic column positions, corresponding to the local polarization vector, are labeled with arrows with orientation displayed in Figure 3f. The correlation length of unit cells with the same polarization vectors, horizontal or <111> directions, in NN-10ST-2LMT (RFE, Figure 3d) is estimated to be 5–8 nm. In contrast, the correlation length in $NNTa_{0.10}$-10ST-2LMT (QLD) with the

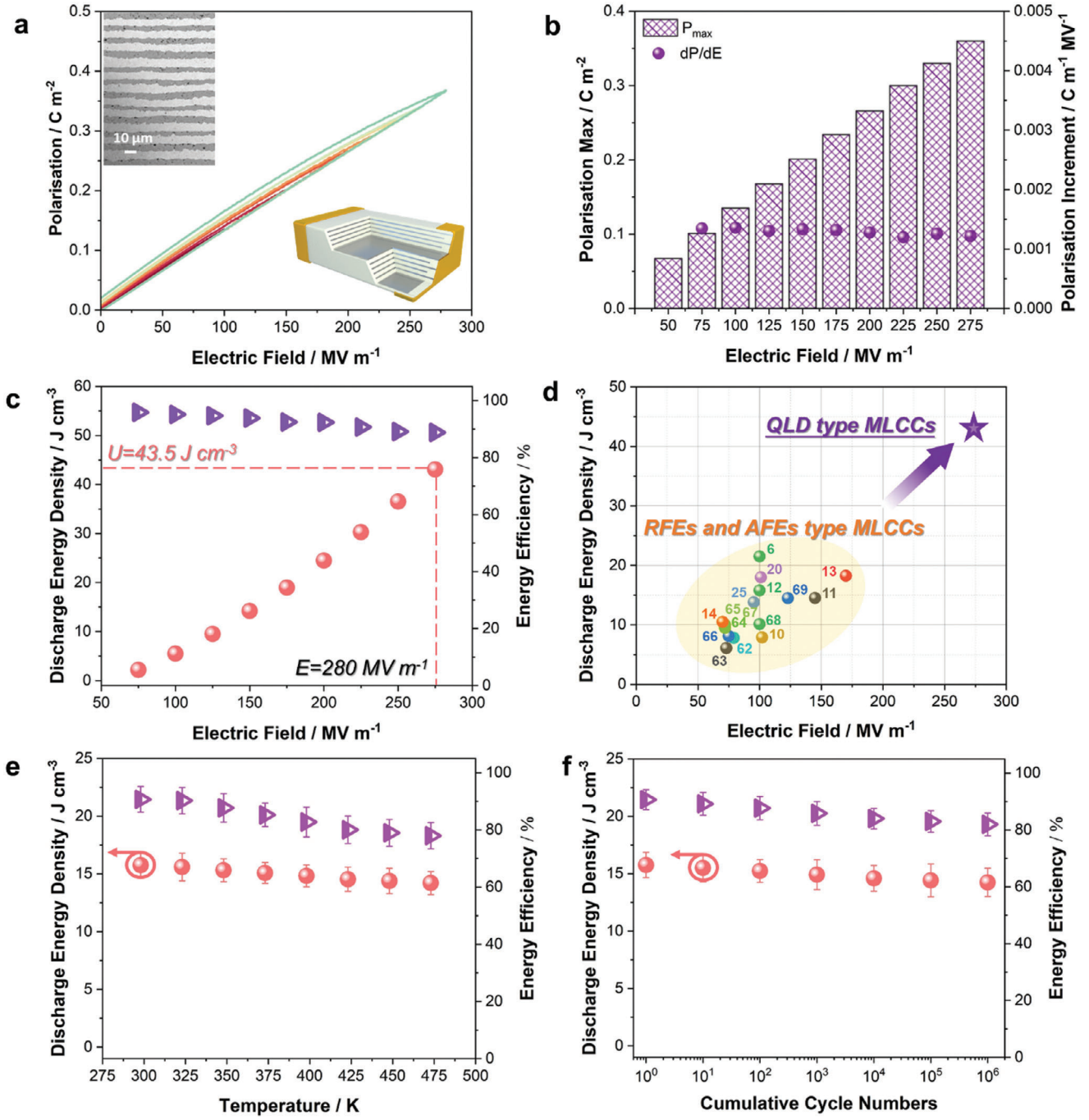

Figure 4. QLD type MLCCs performance. a) Unipolar P–E curves of $NNTa_{0.10}$-10ST-2LMT MLCCs up to the maximum field. b) Polarization maximum and increment as a function of electric field up to 280 MV m^{-1}. c) Energy storage performance up to the maximum field. d) Comparison of QLD behavior MLCCs and "state-of-art" RFE and AFE type MLCCs as the numbers beside the data points are the cited references. Energy storage performance as a function of e) Temperature at 150 MV m^{-1} and f) Cumulative AC cycles at 150 MV m^{-1}.

same polarization vector is only maintained up to 3-unit cells, Figure 3e. The projected polarization angle (Figure 3g) and polarization magnitude (Figure 3h) mappings between NN-10ST-2LMT (RFE) and $NNTa_{0.10}$-10ST-2LMT (QLD) are also compared. The B-site ion displacements are greater and more strongly coupled in NN-10ST-2LMT (RFE), but smaller and more weakly coupled in $NNTa_{0.10}$-10ST-2LMT (QLD). The [110]-oriented atomic resolution HAADF-STEM of $NNTa_{0.10}$-10ST-2LMT (QLD) was also performed, followed by B-site displacements analysis, as shown in Figure S13 (Supporting Information). Similar B-site cation displacement as the data obtained from [001]-oriented grains is evident. Local symmetries are dominated by O structure (potentially local Q phase), Figure S13b (Supporting Information). We demonstrate therefore by direct observation

that nanodomains are not present in the QLD but are apparent in the RFE sample, consistent with the dielectric, P-E, and S-E data.

2.3. $NNTa_{0.10}$-10ST-2LMT Multilayers

Multilayers of $NNTa_{0.10}$-10ST-2LMT (QLD) consisted of ten active ceramic layers with a thickness of ≈6 (±1) µm (measured from the SEM images), Figure S14a (Supporting Information). E_{max} for the QLD type MLCCs reaches 280 (±25) MV m^{-1} to give a P_{max} = 0.38 (±0.03) C m^{-2}, **Figure 4a** and Figure S14b–e (Supporting Information). The P_{max} value here is relatively high for a non-ferroelectric, suggesting short-range, electric field-induced polarization.[61] It is crucial to examine the QLD behavior (dP/dE) of MLCCs, since all high energy density RFE type MLCCs, such as BF-BT-0.08Nd$(Zr_{0.5}Zn_{0.5})O_3$ (U = 10.5 J cm^{-3} at 72 MV m^{-1}),[14] BT-0.06Bi$(Mg_{1/3}Nb_{2/3})O_3$ (U = 6.9 J cm^{-3} at 82 MV m^{-1})[62] and NBT-SBT-0.08Bi$(Mg_{2/3}Nb_{1/3})O_3$ (U = 18 J cm^{-3} at 102 MV m^{-1}),[20] exhibit a significate decrease in dP/dE of > 50% with increasing E, as shown in Figure S15a–c (Supporting Information). The dP/dE of the QLD type MLCCs reported in this study remain 0.0013 (±0.0002) C m^{-1} MV^{-1} from low-field (75 MV m^{-1}) to high-field (280 MV m^{-1}), as illustrated in Figure 4b, Figure S14d,e (Supporting Information). The energy storage performance (evaluated from P-E measurements) of the QLD type MLCCs is U = 43.5 (±2.6) J cm^{-3} with η = 85 (±3) %, Figure 4c, at least twice that of all reported RFE and AFE type MLCCs to date (Figure 4d).[6,10–14,20,25,63–69] The giant U obtained in the QLD type MLCCs thus not only depends on the MLCC's ability to withstand a high E_{max} (associated with homogenous physical and electrical microstructure, low leakage conductivity, and high activation energy) but also the QLD behavior in which dP/dE is almost constant. dP/dE for QLD type MLCCs is lower than in equivalent bulk compositions but nonetheless remains constant from low-field to high field, as illustrated for bulk ceramics in Figure 2c.

Temperature stabilities remain a challenge for all reported RFE[6,12,14,25] and AFE[10,70,71] type MLCCs which routinely experience degradation >15% in U from RT to >150 °C which is attributed to a field-induced increase in polar correlation length (nano-to meso-domain state) and the motion of oxygen vacancies under the application of high electric fields. Temperature-dependent, 25 °C (298 K) to 200 °C (473 K), P-E loops at 150 MV m^{-1} for $NNTa_{0.10}$-10ST-2LMT MLCCs are shown in Figure S15d (Supporting Information). U drops < 10% from ≈15.7 J cm^{-3} (150 MV m^{-1}) at 25 °C (298 K) to ≈14.5 J cm^{-3} at 200 °C (473 K), Figure 4e, with little variation over the measured temperature range, representing to date the best high temperature and temperature stability performance of any high permittivity MLCCs. The absence of large electrostrain (0.12%) minimizes the potential of microcracking and P-E loops (Figure S15e, Supporting Information) at 150 MV m^{-1} exhibit <10% degradation up to 10^6 cycles (Figure 4f). QLD type MLCCs therefore deliver the most reliable, thermal- and fatigue-resistant discharge energy performance (U ≈ 15 J cm^{-3}) at an extremely high electric field (150 MV m^{-1}). Current prototypes use Pt as inner electrodes since the densification temperature (1290 °C) is, at present, too high for more cost-effective electrode solutions such as Ni and Ag/Pd.[72] However, these compositions are both Bi- and Pb-free and should not react with either Ag-Pd or Ni in the manner observed for NBT and BF-based compositions.[73,74] We are therefore confident that reducing the sintering temperature with a suitable glass addition (common practice in the manufacture of BT based MLCCs[5]) should permit the use of lower cost Ag/Pd or Ni internal electrodes in future iterations for scalable manufacturing.

3. Conclusion

In the past decade, lead-free, high energy density capacitors reported have either been RFE type (i.e., BF and NBT based) or AFE-type (i.e., $AgNbO_3$ based) dielectrics. Conventional LDs, such as $CaZrO_3$, Al_2O_3, and $CaTiO_3$, are considered undesirable candidates for high energy MLCCs due to their low ε_r (< 180), low P (< 0.1 C m^{-2}), and U (< 3.5 J cm^{-1}). Multilayers of RFE and AFE compositions have therefore been developed to improve U ($6 \leq U \leq 21$ J cm^{-3}) by optimizing P_{max} (>0.5 C m^{-3}) and E_{max} (>150 MV m^{-1}). MLCCs based on these compositions, however, suffer from poor performance above 125–150 °C and in some cases exhibit large electrostrain. Here, we propose that a third critical factor, dP/dE, is equally as important as P_{max} and E_{max} to deliver high energy density.

Lead-free, $NNTa_{0.10}$-10ST-2LMT MLCCs presented in this study exhibit a near constant dP/dE from low to high field (≈280 MV m^{-1}), typical of QLD behavior but with high ε_r > 500 at ambient. The combination of high E_{max}, P_{max} (ε_r), and constant dP/dE results in an exceptional value of U ≈ 43.5 J cm^{-3} for an MLCC manufactured from tape cast/screen print technology (as opposed to Physical Vapor Deposition, PVD, techniques), accompanied by η ≈ 85%. Importantly, QLD type MLCCs exhibit scant variation in U (< 10% at 150 MV m^{-1}, U ≈ 15 J cm^{-3}) up to > 200 °C and robust resistance to degradation during cycling (<10%). High ε_r (> 500), QLDs therefore offer a promising new approach with respect to RFEs and AFEs in the materials' design and device fabrication of lead-free, high-energy density, ultrahigh voltage, broad temperature stability, and reliable capacitors in power electronics.

4. Experimental Section

Synthesis of NN-10ST Based Ceramics: (0.9-x)$NaNbO_3$-0.1$SrTiO_3$-x$La(Mg_{1/2}Ti_{1/2})O_3$ ($0.00 \leq x \leq 0.06$, NN-10ST-100xLMT) and 0.88$Na(Nb_{1-y}Ta_y)O_3$-0.1$SrTiO_3$-0.02$La(Mg_{1/2}Ti_{1/2})O_3$ ($0.05 \leq y \leq 0.15$, $NNTa_y$-10ST-2LMT), were synthesized using Na_2CO_3, Nb_2O_5, $SrCO_3$, TiO_2, La_2O_3, MgO and Ta_2O_5 as raw materials by a conventional solid-state reaction method. All the raw materials had analytical-grade purity and were dried in a furnace for 8 h to remove any adsorbed water. The dried raw materials were weighed according to their stoichiometry and ball milled for 16 h using Y_2O_3-stabilised ZrO_2 media in isopropanol. The mixed powders were calcined at 850 °C for 2 h and ball milled again for 16 h. The dried calcined powders were mixed with 10 wt% binder (Polyvinyl alcohol, Sigma Aldrich), uniaxially pressed into 10 mm diameter pellets, and sintered at 1300–1330 °C for 3 h in air with additional binder burnout stage at 550 °C for 3 h.

Fabrication of $NNTa_{0.10}$-10ST-2LMT MLCCs: $NNTa_{0.1}$-10ST-2LMT calcined powders were sieved first and ball milled with a binder (polypropylene carbonate, Empower Materials) and a plasticizer (benzylbutyl phthalate, Sigma Aldrich) using Y_2O_3-stabilized ZrO_2 as grinding media in solvent (Methyl Ethyl Ketone, Sigma Aldrich) for 48 h to form a slurry. Ceramic

tapes were fabricated using an MTI MSK-AFA-II tape caster with a single doctor blade. The wet tapes were dried in a fume cupboard for 24 h. Pt electrodes (Sunchemicals) were printed onto the dried tape using a DEK 247 screen printer. The multilayers were fabricated by stacking several tapes layer by layer with an offset, and hot-pressed at 80 °C for 30 min. Each stacked multilayers contained 11 electrodes and 20 unelectroded layers (buffers) above and below the active region to prevent warping. Multilayers were sintered at 1290 °C for 3 h with three additional temperature holds for 3 h on heating at 180, 300, and 600 °C to remove organic binders. Prior to electrical measurements, multilayers were coated with Au termination electrodes on two sides and fired at 850 °C for 2 h in air.

Structural and Microstructural Characterizations: The phase structure of the samples was determined by X-ray diffraction using a Bruker D2 phaser. The morphology of the multilayers was investigated using a FEI Nova Nano 450 scanning electron microscope with an energy-dispersive (EDS) detector. The samples for transmission electron microscope (TEM) study were prepared using a Helios G4 CX focused ion beam thinner. The microstructural domain morphology, selected area electron diffraction (SAED), and dark field images were evaluated using a Talos F200X G2 TEM at an accelerating voltage of 200 kV. The atomic resolution high-angle annular dark-field scanning transmission electron microscope (HAADF-STEM) images were examined using an atomic resolution FEI Titan Cubed Themis G2 spherical aberration corrected STEM. Local distortions corresponding to different symmetries were determined by one B-site cation relative to the center of four A-site cations. The accurate atomic column positions at picometer-precision fitting in the STEM images and subtracted information (including the polarization vector, polarization magnitude, and angles) were performed using customized MATLAB scripts.

Dielectric, Ferroelectric, and Impedance Characterization: Ceramic samples for dielectric and impedance characterization were coated with Au electrodes and fired at 850 °C for 2 h. The temperature and frequency dependence of the dielectric properties (permittivity and tan δ) were collected using an Agilent 4184A Precision LCR Meter (Agilent Technology, California, USA) from room temperature to 500 °C (773 K) and an Agilent E4980A Precision LCR Meter (Agilent Technology, California, USA) with an Oxford Instruments Cryocooler (Oxford Instruments, UK) from −193 °C to room temperature (80 to 300 K), respectively. Impedance spectroscopy (IS) of the ceramics was measured using an Agilent 4980A (Agilent Technology, California, USA) from 20 Hz to 2 MHz and from room temperature to 600 °C (873 K) with an AC voltage of 100 mV. Resistivity of samples was obtained by fitting the experimental IS data using ZView software (Scribner Associates, Inc., Southern Pines, NC). All the IS and LCR data were corrected by a geometric factor (thickness/surface area). Ceramic pellets for ferroelectric measurements were first ground to a thickness of ≈0.2 mm and then sputtered with Au electrodes (Agar Scientific, UK) on both sides with electrode area of 10–12 mm^2. The thicknesses of effective dielectric and Pt layer of MLCC were ≈6 (±1) µm. The electrode area of MLCC was ≈0.3×0.2 cm. P-E and S-E loops were measured using an aixACCT TF 2000E ferroelectric tester at 1 Hz in a temperature range from room temperature to 200 °C (300 to 473 K).

Supporting Information

Supporting Information is available from the Wiley Online Library or from the author.

Acknowledgements

The authors thank the Engineering and Physical Science Research Council grant EP/L017563/1 (Substitution and Sustainability in Functional Materials and Devices), Leverhulme Trust grant "Understanding the mixing and properties of high entropy perovskites", China Scholarship Council No. 202008370166 and Shenzhen Science and Technology Program, No. JCYJ 20220531095802005 for partial funding. The authors also thank the Dame Kathleen Ollerenshaw Fellowship grant "Developing next generation of energy materials and devices" provided by the University of Manchester. The authors also thank the wider support provided by the Functional Materials and Devices group at The University of Sheffield and the useful discussion with Dr Haijun Wu from Xi'an Jiaotong University and Dr Hongfen Ji from Xi'an Technological University.

Conflict of Interest

The authors declare no conflict of interest.

Author Contributions

The work was conceived and designed by X.W., G.W., and I.M.R.; X.W. and G.W. fabricated and characterized (structural and electrical measurements) the bulk ceramics and multilayer capacitors; X.W., X.S., T.H., Z.L., and Z.F. performed microstructural characterization and analysis; Y.F., D.W., L.L., and A.F. assisted electrical measurements and analysis; G.W. and I.M.R. supervised the project; G.W., X.W., D.C.S., and I.M.R. drafted the manuscript, and G.W., I.M.R., and D.C.S. further revised the manuscript.

Data Availability Statement

The data that support the findings of this study are available from the corresponding author upon reasonable request.

Keywords

dP(Polarization)/dE(Electric field), energy storage, high permittivity, multilayer ceramic capacitors, quasi linear dielectric

Received: February 21, 2024
Revised: April 30, 2024
Published online:

[1] P. Simon, Y. Gogotsi, *Nat. Mater.* **2020**, *19*, 1151.
[2] G. Wang, Z. Lu, Y. Li, L. Li, H. Ji, A. Feteira, D. Zhou, D. Wang, S. Zhang, I. M. Reaney, *Chem. Rev.* **2021**, *121*, 6124.
[3] L. Yang, X. Kong, F. Li, H. Hao, Z. Cheng, H. Liu, J.-F. Li, S. Zhang, *Prog. Mater. Sci.* **2019**, *102*, 72.
[4] C. Nies, S. Harris, S. Cygan, *Additional Conferences (Device Packaging, HiTEC, HiTEN, & CICMT)*. **2010**, *2010*, 000244.
[5] M. J. Pan, C. A. Randall, *IEEE Electr. Insul. Mag.* **2010**, *26*, 44.
[6] J. Li, Z. Shen, X. Chen, S. Yang, W. Zhou, M. Wang, L. Wang, Q. Kou, Y. Liu, Q. Li, Z. Xu, Y. Chang, S. Zhang, F. Li, *Nat. Mater.* **2020**, *19*, 999.
[7] J. Kim, S. Saremi, M. Acharya, G. Velarde, E. Parsonnet, P. Donahue, A. Qualls, D. Garcia, L. W. Martin, *Science* **2020**, *369*, 81.
[8] H. Pan, F. Li, Y. Liu, Q. Zhang, M. Wang, S. Lan, Y. Zheng, J. Ma, L. Gu, Y. Shen, P. Yu, S. Zhang, L.-Q. Chen, Y.-H. Lin, C.-W. Nan, *Science* **2019**, *365*, 578.
[9] B. Xu, J. Íñiguez, L. Bellaiche, *Nat. Commun.* **2017**, *8*, 15682.
[10] L.-F. Zhu, L. Zhao, Y. Yan, H. Leng, X. Li, L.-Q. Cheng, X. Xiong, S. Priya, *J. Mater. Chem. A* **2021**, *9*, 9655.
[11] L.-F. Zhu, S. Deng, L. Zhao, G. Li, Q. Wang, L. Li, Y. Yan, H. Qi, B.-P. Zhang, J. Chen, J.-F. Li, *Nat. Commun.* **2023**, *14*, 1166.
[12] Z. Lu, G. Wang, W. Bao, J. Li, L. Li, A. Mostaed, H. Yang, H. Ji, D. Li, A. Feteira, F. Xu, D. Sinclair, D. Wang, S.-Y. Liu, I. Reaney, *Energy Environ. Sci.* **2020**, *13*, 2938.
[13] P. Zhao, Z. Cai, L. Chen, L. Wu, Y. Huan, L. Guo, L. Li, H. Wang, X. Wang, *Energy Environ. Sci.* **2020**, *13*, 4882.

[14] G. Wang, J. Li, X. Zhang, Z. Fan, F. Yang, A. Feteira, D. Zhou, D. C. Sinclair, T. Ma, X. Tan, D. Wang, I. M. Reaney, *Energy Environ. Sci.* **2019**, *12*, 582.
[15] L. Chen, S. Deng, H. Liu, J. Wu, H. Qi, J. Chen, *Nat. Commun.* **2022**, *13*, 3089.
[16] L. Chen, F. Long, H. Qi, H. Liu, S. Deng, J. Chen, *Adv. Funct. Mater.* **2022**, *32*, 2110478.
[17] B. Yang, Y. Zhang, H. Pan, W. Si, Q. Zhang, Z. Shen, Y. Yu, S. Lan, F. Meng, Y. Liu, H. Huang, J. He, L. Gu, S. Zhang, L.-Q. Chen, J. Zhu, C.-W. Nan, Y.-H. Lin, *Nat. Mater.* **2022**, *21*, 1074.
[18] Z. Liu, T. Lu, J. Ye, G. Wang, X. Dong, R. Withers, Y. Liu, *Adv. Mater. Technol.* **2018**, *3*, 1800111.
[19] X. Liu, X. Tan, *Adv. Mater.* **2016**, *28*, 574.
[20] H. Ji, W. Bao, Z. Lu, G. Wang, J. Li, H. Yang, A. Mostaed, L. Li, A. Feteira, F. Xu, D.-J. Li, G. Liu, D. Wang, S.-Y. Liu, I. M. Reaney, *Energy Storage Mater.* **2021**, *38*, 113.
[21] Q. Li, L. Chen, M. R. Gadinski, S. Zhang, G. Zhang, H. U. Li, E. Iagodkine, A. Haque, L.-Q. Chen, T. N. Jackson, Q. Wang, *Nature* **2015**, *523*, 576.
[22] B. Chu, X. Zhou, K. Ren, B. Neese, M. Lin, Q. Wang, F. Bauer, Q. M. Zhang, *Science* **2006**, *313*, 334.
[23] L. Li, J. Cheng, Y. Cheng, T. Han, Y. Liu, Y. Zhou, G. Zhao, Y. Zhao, C. Xiong, L. Dong, Q. Wang, *Adv. Mater.* **2021**, *33*, 2102392.
[24] J. Chen, Y. Zhou, X. Huang, C. Yu, D. Han, A. Wang, Y. Zhu, K. Shi, Q. Kang, P. Li, P. Jiang, X. Qian, H. Bao, S. Li, G. Wu, X. Zhu, Q. Wang, *Nature* **2023**, *615*, 62.
[25] G. Wang, Z. Lu, H. Yang, H. Ji, A. Mostaed, L. Li, Y. Wei, A. Feteira, S. Sun, D. C. Sinclair, D. Wang, I. M. Reaney, *J. Mater. Chem. A* **2020**, *8*, 11414.
[26] T. Tsurumi, M. Shono, H. Kakemoto, S. Wada, K. Saito, H. Chazono, *Jpn. J. Appl. Phys.* **2005**, *44*, 6989.
[27] L. Yang, X. Kong, Z. Cheng, S. Zhang, *J. Mater. Chem. A* **2019**, *7*, 8573.
[28] W. S. Lee, C. Y. Su, Y. C. Lee, S. P. Lin, T. Yang, *Jpn. J. Appl. Phys.* **2006**, *45*, 5853.
[29] B. Luo, X. Wang, E. Tian, H. Song, H. Wang, L. Li, *ACS Appl. Mater. Interfaces* **2017**, *9*, 19963.
[30] H. Y. Zhou, X. Q. Liu, X. L. Zhu, X. M. Chen, *J. Am. Ceram. Soc.* **2018**, *101*, 1999.
[31] Y. Pu, W. Wang, X. Guo, R. Shi, M. Yang, J. Li, *J. Mater. Chem. C* **2019**, *7*, 14384.
[32] P. Zhao, Z. Cai, L. Wu, C. Zhu, L. Li, X. Wang, *J. Adv. Ceram.* **2021**, *10*, 1153.
[33] H. Pan, S. Lan, S. Xu, Q. Zhang, H. Yao, Y. Liu, F. Meng, E.-J. Guo, L. Gu, D. Yi, X. Renshaw Wang, H. Huang, J. L. MacManus-Driscoll, L.-Q. Chen, K.-J. Jin, C.-W. Nan, Y.-H. Lin, *Science* **2021**, *374*, 100.
[34] T. Li, S. Deng, R. Zhu, J. Yang, S. Xu, Y. Dong, H. Liu, C. Huo, P. Gao, Z. Luo, O. Diéguez, H. Huang, S. Liu, L.-Q. Chen, H. Qi, J. Chen, *J. Am. Chem. Soc.* **2024**, *146*, 1926.
[35] H. Zhang, B. Yang, H. Yan, I. Abrahams, *Acta Mater.* **2019**, *179*, 255.
[36] M.-H. Zhang, L. Fulanović, C. Zhao, J. Koruza, *J. Materiomics* **2023**, *9*, 1.
[37] A. Xie, H. Qi, R. Zuo, A. Tian, J. Chen, S. Zhang, *J. Mater. Chem. C* **2019**, *7*, 15153.
[38] A. Xie, H. Qi, R. Zuo, *ACS Appl. Mater. Interfaces* **2020**, *12*, 19467.
[39] D. Zheng, R. Zuo, *J. Eur. Ceram. Soc.* **2017**, *37*, 413.
[40] H. Yang, H. Qi, R. Zuo, *J. Eur. Ceram. Soc.* **2019**, *39*, 2673.
[41] A. Tian, R. Zuo, H. Qi, M. Shi, *J. Mater. Chem. A* **2020**, *8*, 8352.
[42] N. Luo, K. Han, M. J. Cabral, X. Liao, S. Zhang, C. Liao, G. Zhang, X. Chen, Q. Feng, J.-F. Li, Y. Wei, *Nat. Commun.* **2020**, *11*, 4824.
[43] L. Yang, X. Kong, Q. Li, Y.-H. Lin, S. Zhang, C.-W. Nan, *ACS Appl. Mater. Interfaces* **2022**, *14*, 32218.
[44] Y. Han, I. M. Reaney, R. L. Johnson-Wilke, M. B. Telli, D. S. Tinberg, I. Levin, D. D. Fong, T. T. Fister, S. K. Streiffer, S. Trolier-McKinstry, *J. Appl. Phys.* **2010**, *107*, 123517.
[45] A. M. Glazer, *Acta Crystallogr. B* **1972**, *28*, 3384.
[46] A. A. Bokov, Z. G. Ye, *J. Mater. Sci.* **2006**, *41*, 31.
[47] R. D. Shannon, *Acta Crystallogr. A* **1976**, *32*, 751.
[48] S. Kamba, V. Goian, V. Bovtun, D. Nuzhnyy, M. Kempa, M. Spreitzer, J. König, D. Suvorov, *Ferroelectrics* **2012**, *426*, 206.
[49] X. Wang, Y. Fan, Z. Bin, A. Mostaed, L. Li, A. Feteira, D. Wang, D. C. Sinclair, G. Wang, I. M. Reaney, *J. Eur. Ceram. Soc.* **2022**, *42*, 7381.
[50] D. Li, D. Zhou, D. Wang, W. Zhao, Y. Guo, Z. Shi, T. Zhou, S.-K. Sun, C. Singh, S. Trukhanov, A. S. B. Sombra, *Small* **2023**, *19*, 2206958.
[51] H. Yang, Z. Lu, L. Li, W. Bao, H. Ji, J. Li, A. Feteira, F. Xu, Y. Zhang, H. Sun, Z. Huang, W. Lou, K. Song, S. Sun, G. Wang, D. Wang, I. M. Reaney, *ACS Appl. Mater. Interfaces* **2020**, *12*, 43942.
[52] H. Qi, A. Xie, A. Tian, R. Zuo, *Adv. Energy Mater.* **2020**, *10*, 1903338.
[53] D. Li, D. Zhou, D. Wang, W. Zhao, Y. Guo, Z. Shi, *Adv. Funct. Mater.* **2022**, *32*, 2111776.
[54] M. Zhang, H. Zhang, Q. Jiang, F. Gao, R. Chen, D. Zhang, M. J. Reece, B. Yang, G. Viola, H. Yan, *ACS Appl. Mater. Interfaces* **2021**, *13*, 53492.
[55] D. I. Woodward, I. M. Reaney, *Acta Crystallogr. B* **2005**, *61*, 387.
[56] I. Levin, J. C. Woicik, A. Llobet, M. G. Tucker, V. Krayzman, J. Pokorny, I. M. Reaney, *Chem. Mater.* **2010**, *22*, 4987.
[57] I. M. Reaney, *Ferroelectrics* **1995**, *172*, 115.
[58] A. Xie, R. Zuo, Z. Qiao, Z. Fu, T. Hu, L. Fei, *Adv. Energy Mater.* **2021**, *11*, 2101378.
[59] V. Dimitrov, S. Sakka, *J. Appl. Phys.* **1996**, *79*, 1736.
[60] A. De Backer, K. H. W. van den Bos, W. Van den Broek, J. Sijbers, S. Van Aert, *Ultramicroscopy* **2016**, *171*, 104.
[61] H. Zhang, H. Gidden, T. G. Saunders, N. Liu, V. Aurallo-Peters, X. Xu, M. Palma, M. J. Reece, I. Abrahams, H. Yan, Y. Hao, *Chem. Mater.* **2020**, *32*, 10120.
[62] H. Yang, W. Bao, Z. Lu, L. Li, H. Ji, Y. Huang, F. Xu, G. Wang, D. Wang, *J. Mater. Res.* **2021**, *36*, 1285.
[63] H. Ogihara, C. A. Randall, S. Trolier-McKinstry, *J. Am. Ceram. Soc.* **2009**, *92*, 1719.
[64] J. Li, F. Li, Z. Xu, S. Zhang, *Adv. Mater.* **2018**, *30*, 1802155.
[65] G. Wang, Z. Lu, J. Li, H. Ji, H. Yang, L. Li, S. Sun, A. Feteira, H. Yang, R. Zuo, D. Wang, I. M. Reaney, *J. Eur. Ceram. Soc.* **2020**, *40*, 1779.
[66] Z. Cai, H. Wang, P. Zhao, L. Chen, C. Zhu, K. Hui, L. Li, X. Wang, *Appl. Phys. Lett.* **2019**, *115*, 023901.
[67] Z. Cai, C. Zhu, H. Wang, P. Zhao, L. Chen, L. Li, X. Wang, *J. Mater. Chem. A* **2019**, *7*, 14575.
[68] P. Zhao, H. Wang, L. Wu, L. Chen, Z. Cai, L. Li, X. Wang, *Adv. Energy Mater.* **2019**, *9*, 1803048.
[69] P. Zhao, L. Chen, L. Li, X. Wang, *J. Mater. Chem. A* **2021**, *9*, 25914.
[70] L.-F. Zhu, Y. Yan, H. Leng, X. Li, L.-Q. Cheng, S. Priya, *J. Mater. Chem. C* **2021**, *9*, 7950.
[71] L. Fulanović, M.-H. Zhang, Y. Fu, J. Koruza, J. Rödel, *J. Eur. Ceram. Soc.* **2021**, *41*, 5519.
[72] L. Gao, H. Guo, S. Zhang, C. A. Randall, *Actuators* **2016**, *5*, 8.
[73] S. F. Wang, W. Huebner, *J. Am. Ceram. Soc.* **1992**, *75*, 2339.
[74] S.-T. Kuo, W.-H. Tuan, Y.-W. Lao, C.-K. Wen, H.-R. Chen, *Int. J. Appl. Ceram. Technol.* **2009**, *6*, 223.